Hindawi
Journal of Sensors
Volume 2022, Article ID 8969479, 12 pages
https://doi.org/10.1155/2022/8969479

Research Article

Fault Location Method in Nonsolid-Earthed Network Based on Spatial Domain Image Fusion and Convolution Neural Network

Sizu Hou and Wei Guo

School of Electrical and Electronic Engineering, North China Electric Power University, Baoding 071003, China

Correspondence should be addressed to Wei Guo; xiaoshenghameng@163.com

Received 7 October 2021; Revised 19 January 2022; Accepted 21 January 2022; Published 7 February 2022

Academic Editor: Zahid Mehmood

Copyright © 2022 Sizu Hou and Wei Guo. This is an open access article distributed under the Creative Commons Attribution License, which permits unrestricted use, distribution, and reproduction in any medium, provided the original work is properly cited.

Given that the single-terminal traveling wave location method has significant errors, a novel fault location method based on the spatial domain image fusion and convolutional neural network (CNN) is proposed. Firstly, the three-phase traveling wave can be decoupled by the phase-mode transformation matrix for obtaining the line-mode component of the traveling wave. Secondly, the 1D line-mode traveling wave can be converted into a 2D image by the Gramian angular field (GAF). The 1D line-mode component can be mapped into the color, point, line, and other characteristic parameters of the 2D image. In order to expand the invisible information of the line-mode traveling wave, the images obtained by the Gramian angular summation field (GASF) and Gramian angular difference field (GADF) are weighted and fused. Finally, the CNN can be used to autonomously mine the characteristic parameters of the weight-fusion image and realize fault location. The simulation results show that the proposed method does not need to be considered in the traveling wave head and the traveling wave speed. The localization method is not affected by fault time, fault distance, or transition resistance factors. It possesses high reliability with an absolute range error of no more than 200 m.

1. Introduction

The medium-voltage distribution network usually adopts a small current grounding system (SCGS) in China, and the single-phase grounding fault has become one of the crucial factors influencing the reliability of the power supply [1, 2]. Fast and accurate fault location technology can reduce power outage range and power outage time [3]. It has an essential significance for improving the safety, reliability, and economy of the distribution network.

The distribution network structures mostly are arborescent radiation patterns. The model has many branches and short line lengths. When the single-phase grounding fault occurs in the small current grounding system, the fault signal presents nonlinear, faint, complexity, and other features. These factors can give the challenge for fault location. At present, the fault location methods can be roughly divided into several ways, such as fault analysis method, artificial intelligence method, signal injection method, traveling wave method, and impedance method. At the beginning of fault location, the distribution network system lines were considered geometrically symmetrical using symmetrical component-based methodologies [4]. However, symmetrical component-based analysis was applied only to the balanced system. Elkalashy and colleagues [5] used a controlled thyristor to generate a disturbance signal, achieving the wave distance measurement. However, the technique must inject a signal into the neutral point. It can only be used in the neutral point grounding by arc suppression coil and cannot be used in the neutral point ungrounded system. Liao [6] used the substation voltage and current quantities to construct the bus impedance matrix, through which the fault location can be yielded. However, the method needs to know the distribution network parameters and topological structures in advance. Sun and colleagues [7] presented an automated outage mapping method for the automatic faulted line section location. The method needs to collect much customer electric information, and the process is relatively complicated. Sapountzoglou et al. [8] used the gradient boosting trees to establish a fault diagnosis for the low-voltage smart

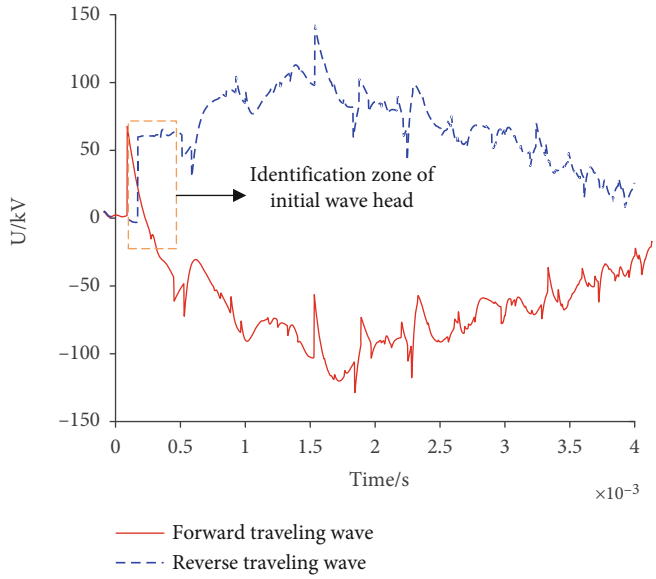

Figure 1: Direction traveling waves of voltage-mode component.

distribution network. The fixed number of interpolations replaces the measurements of a particular branch. This model adapts to changes in the network topology to some extent but does not accurately locate the faulty segment. Teng et al. [9] used the relationship matrix to locate the faulted line sections. The matrix method is easy to realize. However, when the topology changes, the network matrix must be regenerated, demanding large-scale computation quality. One of the most effective methods to calculate the distance-to-fault is the traveling wave method [10, 11]. The uncertainty of fault traveling velocity and arriving time of fault initial traveling wave can affect the accuracy of the location. Karmacharya and Gokaraju [12] used the wavelet-based frequency characteristics to locate the fault sections. But the wrong selection of the decomposition scale and wavelet basis function may obtain erroneous fault location. Machine learning has broad prospects in fault diagnosis. Many intelligent fault diagnosis models have been proposed [13, 14]. Luo et al. [15] built the stack autoencoder (SAE) regression model to constitute the relationship between fault features and fault locations, which can realize the end-to-end faulted line location. Mirzaei and colleagues [16] used the discrete wavelet transform to extract the features of fault voltage, and the generated features are used to train the deep neural networks for obtaining the faulted line segments. Luo et al. [17] combined SAE with signal phase information to realize the fault range finding for the multiterminal transmission line.

Rapid and precise fault location in the distribution network can effectively reduce fault detection and outage time, reduce economic losses, and improve power supply reliability. This article focuses on solving the problem of the distribution network fault location. The main contributions of this article are summarized as follows:

(1) The 1D traveling wave signal can be converted into the 2D image by Gramian angular field (GAF). We used the spatial domain image fusion method to reinforce the invisible information of the traveling wave signal. The signal-to-image method can be beneficial to the convolutional neural network (CNN)

(2) The CNN network structure is designed for fault location in the distribution network. The CNN can mine the image features autonomously, without human extraction of features, avoiding human factor interference

(3) The difference from the traditional single-terminal traveling wave location method, the proposed method does not require detecting the wave head and speed of the traveling wave. It can improve the distance-measuring accuracy

The paper can be divided into the following sections. The phase-mode transformation is introduced in Section 2. In Section 3, the signal-to-image conversion method is proposed. Section 4 describes the fault location based on GAF-CNN. Section 5 shows the results of the fault-ranging experiments.

2. Phase-Mode Transformation

2.1. Characteristics of Traditional Traveling

2.1.1. Wave Fault Location. The traditional traveling wave location is based on arriving time of fault initial traveling wave and fault traveling wave velocity [18, 19]. The method is heavily dependent on the first traveling wave head [20]. Figure 1 provides the direction traveling waves of the voltage-mode component. As can be seen in Figure 1, the duration time of the initial wave head is extremely short. The traveling wave location methods are easily affected by the high resistance earth fault, noise, and other harsh grounding conditions.

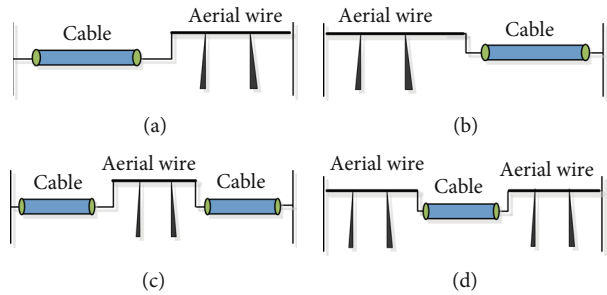

Figure 2: Types of hybrid line consisting of cable and aerial wire.

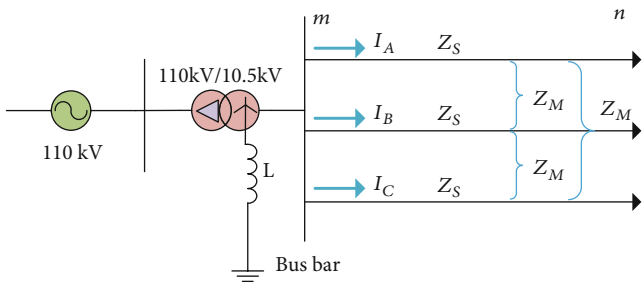

Figure 3: Diagram of the three-phase system.

Figure 2 depicts four types of hybrid lines consisting of cable and aerial wire. For the hybrid transmission line, the influence effect of several factors are as follows: (1) Due to impedance-mismatching between the cable and aerial wire, the traveling wave signal can reflect at the connection point, affecting the effect of the fault location. (2) As the wave velocity of the front and the back of the junction point of the hybrid line consisting of cable and aerial wire is different, the location of the junction point needs to be precisely recognized.

As the traveling wave abruptly changes at the junction point of the hybrid line consisting of cable and aerial wire, we proposed an approach that does not consider the location of the traveling wave head and traveling wave speed. The proposed method only considers the traveling wave per se of characteristics.

2.2. Phase-Mode Transformation Matrix of Three-Phase System. Different phase-mode transformation matrices may affect the effectiveness of the fault location [21]. The diagram of the three-phase system is shown in Figure 3. $\dot{I}_A$, $\dot{I}_B$, and $\dot{I}_C$ can denote the three-phase current phase quantity; m and n represent the head-end of the line and the end of the line, respectively; Z_S and Z_M represent the mutual impedance and the self-impedance, respectively.

For the three-phase system shown in Figure 3, there is a complex electromagnetic coupling between the conductors of each phase of the power system, which needs to be decoupled using the phase mode transformation method in order to simplify the analytical calculations as

$$\begin{aligned}[u]_m &= [T]^{-1}[u]_\varphi,\\ [i]_m &= [T]^{-1}[i]_\varphi,\end{aligned} \tag{1}$$

where $[u]_m$ represents the modal voltage vector, $[i]_m$ denotes the modal current vector, and T is the mode transformation matrix. The mode transformation matrix T and the inverse matrix T^{-1} can be defined as [22]

$$\begin{aligned}T &= \frac{1}{15}\begin{pmatrix}5 & 5 & 5\\ 5 & -1 & -4\\ 5 & -4 & -1\end{pmatrix},\\ T^{-1} &= \begin{pmatrix}1 & 1 & 1\\ 1 & 2 & -3\\ 1 & -3 & 2\end{pmatrix}.\end{aligned} \tag{2}$$

The mode transformation matrix T can transform the current vectors into a modal form, as shown in

$$\begin{pmatrix}\dot{I}_0\\ \dot{I}_1\\ \dot{I}_2\end{pmatrix} = \begin{pmatrix}1 & 1 & 1\\ 1 & 2 & -3\\ 1 & -3 & 2\end{pmatrix}\begin{pmatrix}\dot{I}_A\\ \dot{I}_B\\ \dot{I}_C\end{pmatrix}, \tag{3}$$

where $\dot{I}_0$, $\dot{I}_1$, and $\dot{I}_2$ represent the current modulus components of 0, 1, and 2.

Table 1 provides the current modulus components under all kinds of fault types. In Table 1, it is evident that the modulus values obtained by applying the phase-mode transformation matrix T are the nonnull value for any fault types. Hence, modulus 1 or modulus 2 can accomplish the fault analysis.

3. Signal-to-Image Conversion

3.1. Imaging Line-Mode Component. In order to obtain the 2D image of the traveling wave component, the Gramian angular field (GAF) [23, 24] is used to encode mode 2 obtained by Equation (11). In the traditional Cartesian coordinate system, the time domain signal is a typical 1D signal. The x-axis direction can represent the time value, and the y-axis direction can represent the signal amplitude. The time-domain signal can be represented in a polar coordinate system. Given a time series $X = \{x_1, x_2, x_3, x_n\}$, the normalization method of $[-1, 1]$ can be used

Table 1: Current modulus components under all kinds of fault types.

Fault types	Phase boundary conditions	Modulus 1	Modulus 2
AG	$\dot{I}_B = \dot{I}_C = 0$	$\dot{I}_A$	$\dot{I}_A$
BG	$\dot{I}_A = \dot{I}_C = 0$		$-3\dot{I}_B$
CG	$\dot{I}_A = \dot{I}_B = 0$	$-3\dot{I}_C$	$2\dot{I}_C$
AB	$\dot{I}_C = 0, \dot{I}_C = -\dot{I}_B$	$\dot{I}_B$	$-4\dot{I}_B$
BC	$\dot{I}_A = 0, \dot{I}_B = -\dot{I}_C$	$5\dot{I}_B$	$-5\dot{I}_B$
AC	$\dot{I}_B = 0, \dot{I}_C = -\dot{I}_A$	$4\dot{I}_A$	$-\dot{I}_A$
ABG	$\dot{I}_C = 0$	$\dot{I}_A + 2\dot{I}_B$	$\dot{I}_A$-$3\dot{I}_B$
ACG	$\dot{I}_B = 0$	$\dot{I}_A - 3\dot{I}_C$	$\dot{I}_A + 2\dot{I}_C$
BCG	$\dot{I}_A = 0$	$2\dot{I}_B - 3\dot{I}_C$	$-3\dot{I}_B + 2\dot{I}_C$
ABC	$\dot{I}_A + \dot{I}_B + \dot{I}_C = 0$	$\dot{I}_B - 4\dot{I}_C$	$-4\dot{I}_B + \dot{I}_C$

to normalize the time series X as

$$\tilde{x}_i = \frac{(x_i - \max(X)) + (x_i - \min(X))}{\max(X) - \min(X)}. \tag{4}$$

The normalized time series can be transformed by using the polar coordinate transformation. The magnitude can be calculated as the cosine value of the polar coordinate system, and the timestamp can be used as the radius. The process of polar coordinate conversion can be defined as

$$\begin{cases} \theta_i = \arccos(\tilde{x}_i), -1 \le \tilde{x}_i \le 1, \tilde{x}_i \in \tilde{X}, \\ r_i = \dfrac{t_i}{n}, \end{cases} \tag{5}$$

where θ_i represents the polar angle, t_i denotes the timestamp of the i^{th} time series, r_i is the radius of the polar coordinate, and $\tilde{X}$ is the rescaled time series in polar coordinates.

Since time series has been transformed within polar coordinates, it is easy to mine the correlation between different moment points by the angle of each moment point. The GAF can generate two types of images by using different equations [25, 26]. Equation (7) defines the Gramian angular summation field (GASF), and Equation (9) defines the Gramian angular difference field (GADF).

$$\text{GASF} = \begin{pmatrix} \cos(\theta_1 + \theta) & \cdots & \cos(\theta_1 + \theta_n) \\ \vdots & \ddots & \vdots \\ \cos(\theta_n + \theta_1) & \cdots & \cos(\theta_n + \theta_n) \end{pmatrix}, \tag{6}$$

$$\text{GASF} = \tilde{X}^T \cdot \tilde{X} - \sqrt{I - \tilde{X}^2}^T \cdot \sqrt{I - \tilde{X}^2}, \tag{7}$$

$$\text{GADF} = \begin{pmatrix} \sin(\theta - \theta_2) & \cdots & \sin(\theta_1 - \theta_n) \\ \vdots & \ddots & \vdots \\ \sin(\theta_n - \theta_1) & \cdots & \sin(\theta_n - \theta_n) \end{pmatrix}, \tag{8}$$

$$\text{GADF} = \sqrt{I - \tilde{X}^2}^T \cdot \tilde{X} - \tilde{X}^T \cdot \sqrt{I - \tilde{X}^2}, \tag{9}$$

where I is the unit vector. By redefining the vector inner-product $<x, y> = x \cdot y - \sqrt{1 - x^2} \cdot \sqrt{1 - y^2}$ and $<x, y> = \sqrt{1 - x^2} \cdot y - x \cdot \sqrt{1 - y^2}$, the Gramian matrix G can be expressed as

$$G = \begin{pmatrix} <\tilde{x}_1, \tilde{x}_1> & <\tilde{x}_1, \tilde{x}_2> & \cdots & <\tilde{x}_1, \tilde{x}_n> \\ <\tilde{x}_2, \tilde{x}> & <\tilde{x}_2, \tilde{x}_2> & \cdots & <\tilde{x}_2, \tilde{x}_n> \\ \vdots & \vdots & \ddots & \vdots \\ <\tilde{x}_n, \tilde{x}_1> & <\tilde{x}_n, \tilde{x}_2> & \cdots & <\tilde{x}_n, \tilde{x}_n> \end{pmatrix}. \tag{10}$$

The main diagonal elements of the GAF can store the original values for all moments in the time series. The i^{th} row and j^{th} column of the matrix can represent the correlation coefficient between the i^{th} moment and the j^{th} moment. The GAF can effectively represent the time correlation between different data points. For an original time series with length n, the size of the obtained GAF matrix is $n \times n$. If n is too big, the dimension of the obtained matrix is over large.

The paper used the piecewise aggregate approximation (PAA) to reduce the dimension of the original time series. PAA is to segment the long time series uniformly and then calculate the mean values of each segment. The mean values can become a new data reduction representation [27]. In the case of guaranteeing comprehensive information for the original time series, the length of the time series is reduced by the PAA. Figure 4 provides the procedure of signal-to-image conversion.

The method of the signal-image conversion has two major advantages as follows:

(1) The relationship between the 1D signal and the 2D image is double-mapping relation, which does not lose any information of the 1D signal

(2) It can maintain the time dependence of the signal. The texture information and color distribution of the 2D image can reflect the invisible information of the 1D signal

3.2. Spatial Domain Image Fusion. Figure 5 provides the density histograms of the outputs of the GASF matrix and GADF matrix. As can be seen in Figure 5, the distribution of the GASF is different from that of the GADF. Hence, in order to make full use of the fault information, the images generated by GASF and GADF can be fused by the weighted average fusion algorithm. The fusion process is shown in Figure 6.

By integrating the complementary information, image fusion can reduce or inhibit the impact of the single,

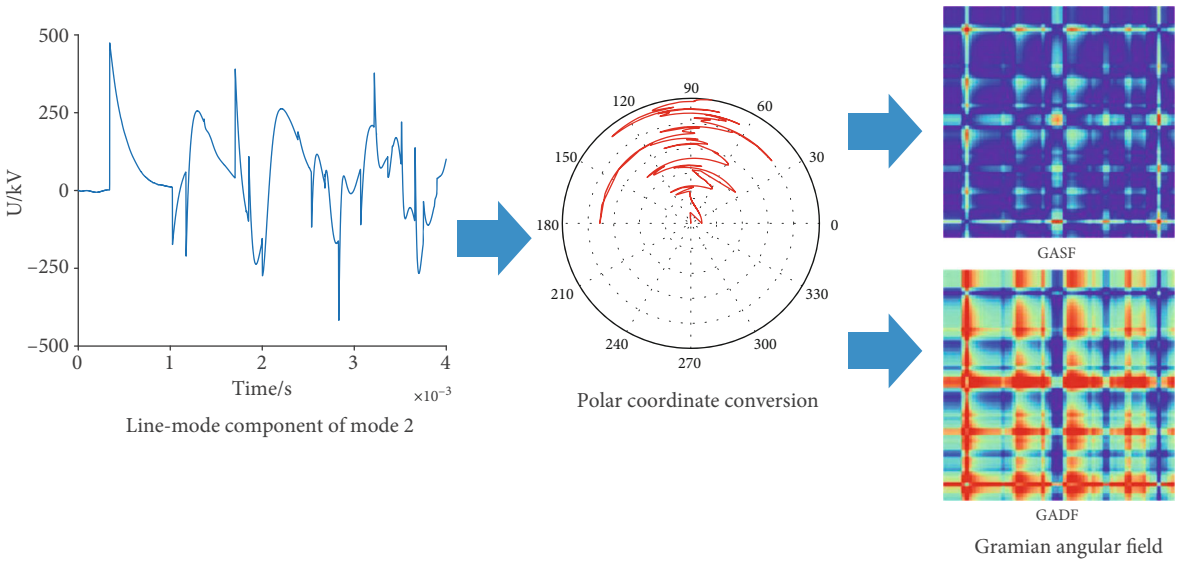

Figure 4: The procedure of signal-image conversion.

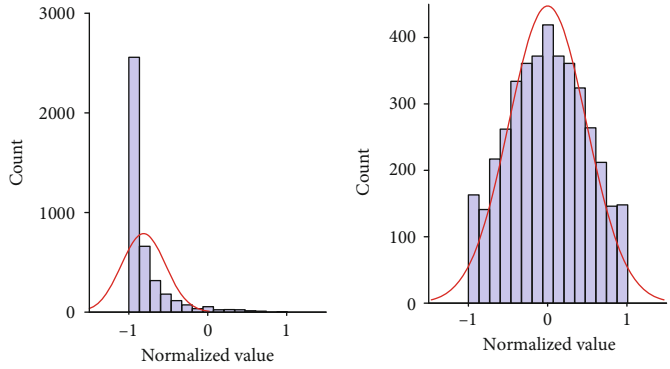

(a) GASF matrix density (b) GADF matrix density

Figure 5: The density histograms of the outputs of the GASF matrix and GADF matrix.

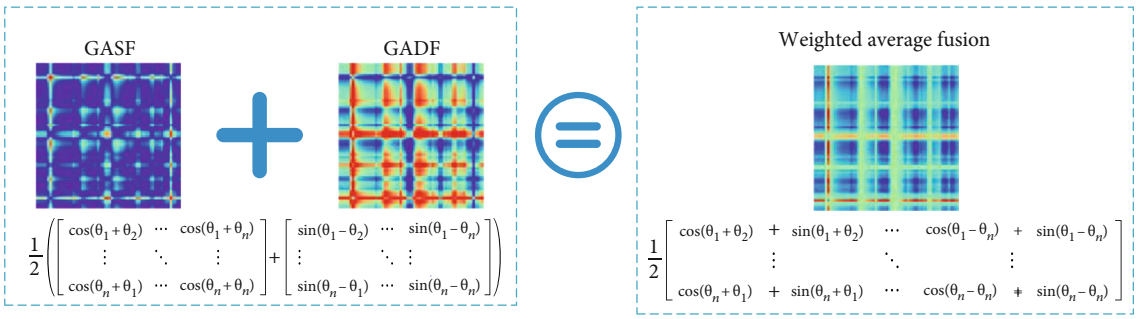

Figure 6: Fusion process of the GASF matrix and GADF matrix.

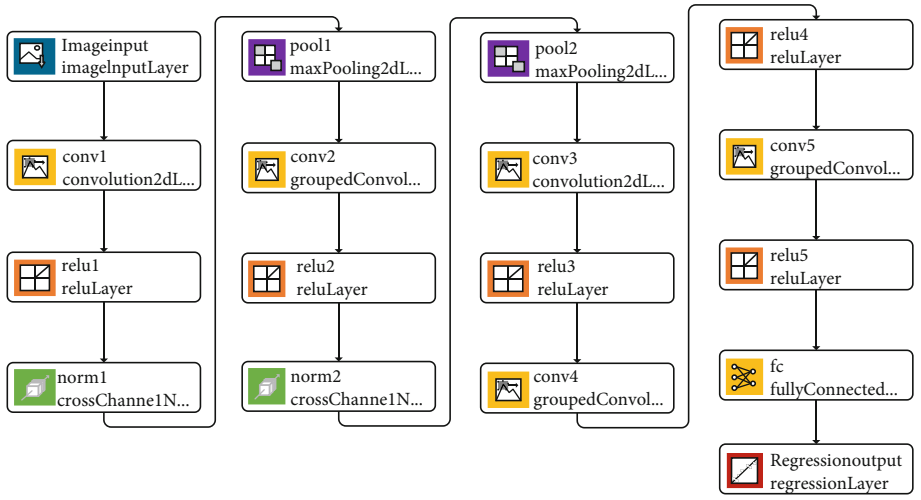

Figure 7: Fault location model based on GAF and CNN.

Table 2: Parameters of fault location model based on GAF and CNN.

Layer name	Structural parameters	Output size
Input layer	64×64	64×64
Convolution lay	$96@11 \times 11$, Stde = [4], "Valid"	$14 \times 14 \times 96$
Activation layer 1	ReLu	$14 \times 14 \times 96$
Normalization layer 1	Local response norm	$14 \times 14 \times 96$
Pooling layer 1	Max pooling 3×3	$6 \times 6 \times 96$
Convolution layer 2	2 groups of 128 $5 \times 5 \times 48$, Stride = [2], "Same"	$6 \times 6 \times 256$
Activation layer 2	ReLu	$6 \times 6 \times 256$
Normalization layer 2	Local response norm	$6 \times 6 \times 256$
Pooling layer 2	Max pooling 3×3	$2 \times 2 \times 256$
Convolution layer 3	$384@3 \times 3 \times 256$, Stride = [1], "Same"	$2 \times 2 \times 384$
Activation layer 3	ReLu	$2 \times 2 \times 384$
Convolution layer 4	2 groups of 192 $5 \times 5 \times 48$, Stride = [1], "Same"	$2 \times 2 \times 384$
Activation layer 4	ReLu	$2 \times 2 \times 384$
Convolution layer 5	2 groups of $13 \times 3 \times 192$, Stride = [1], "Same"	$2 \times 2 \times 256$
Activation layer 5	ReLu	$2 \times 2 \times 256$
Fully connected layer	1 neuron	$1 \times 1 \times 1$
Regression layer	Distance-to-fault	1

repetitive information on the perceived objects. The image fusion can use the various characteristics of the fault signal in the maximum limit. The method can provide a basis for applying deep learning algorithms in fault diagnosis.

4. Fault Location Based on GAF-CNN

4.1. CNN Structure of Fault Location. The convolution neural network (CNN) is a hierarchical neural network [28]. CNN can have significant potential advantages in both feature extraction and model fitting [29]. It has been applied in object detection, image processing, and natural language processing with notable success [30, 31]. The basic structure of the CNN is mainly composed of the input layer, convolution layer, pooling layer, fully connected layer, and output layer. The fault location model based on GAF and CNN is shown in Figure 7. Table 2 provides the parameters of the fault location model based on GAF and CNN. In Table 2, "Valid" represents the valid padding, and "Same" denotes the same padding. In order to cope with the problem that the traditional single-ended traveling wave ranging method is affected by wave speed and pseudo wave head, the paper proposes a single-ended traveling wave fault location method for distribution networks that combines traveling wave theory, GAF, and CNN. The method locates the fault location without considering the wave head and wave speed of the traveling waves.

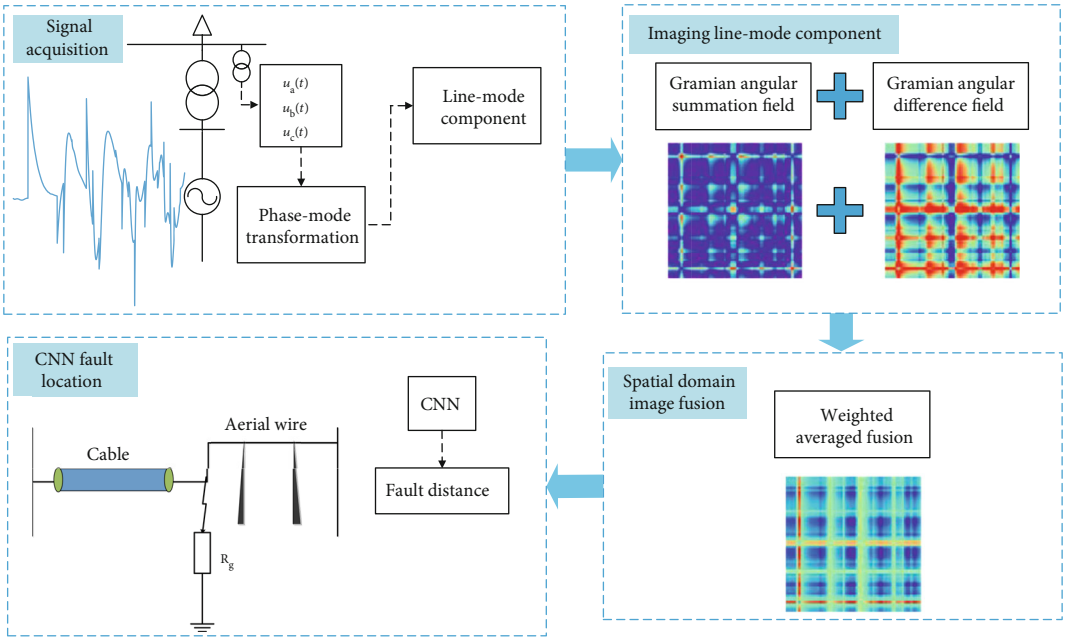

Figure 8: Flowchart of fault location.

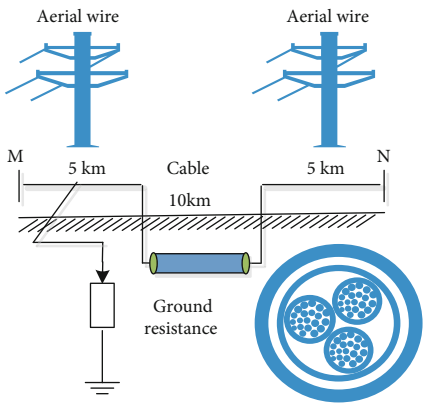

Figure 9: Structure map of hybrid line.

4.2. Fault Location Process. The fault range-measurement method in this paper includes four procedures: signal acquisition, imaging line-mode component, spatial domain image fusion, and CNN fault location. The method does not need to detect the traveling wave head and does not need to know the traveling wave speed. The method is solely focused on the feature of the line-mode component itself. Figure 8 provides the flowchart of the fault location. The step-by-step procedure can be described as follows:

(1) The sampling frequency is 1 MHz. In a postfault distribution network, the phase voltage vectors of the head-end distribution line can be collected, which are converted to the mode vectors by the phase-mode transformation

(2) The line-mode component of mode 2 can be converted into the image by the Gramian angular summation field and the Gramian angular difference field

Table 3: Parameters of training samples.

Fault types	Sample size	Ground resistance	Fault close angle
AG			
BG		0 ~ 1000 Ω	0°, 30°, 60°, 90°, 120°, 150°
CG			

(3) The images generated by GASF and GADF can be fused by the spatial domain image fusion. The weighted average fusion algorithm can make full use of the fault information. The details of the fusion image are more abundant than the original image, and the edge is more clear than the original image. The fusion image can fully reflect the fault characteristics in the distribution network

(4) The fusion images can be used as the input of the CNN. We establish a corresponding relationship between the fault information and feature information by convolution layer, activation layer, normalization layer, pooling layer, fully connected layer, and regression layer. The output of the CNN can achieve the fault location. Some parameters need to be set before training the CNN model: "Solver", adam; "InitialLearnRate", 0.001; "LearnRateDropFactor", 0.005; "LearnRateDropPeriod", 10; "L2Regularization", 0.004, "MaxEpochs", 15; and "MiniBatchSize", 10

5. Experimental Results and Analysis

5.1. Experiment Dataset. Since deep learning requires massive data as support to generate the ideal model by sufficient

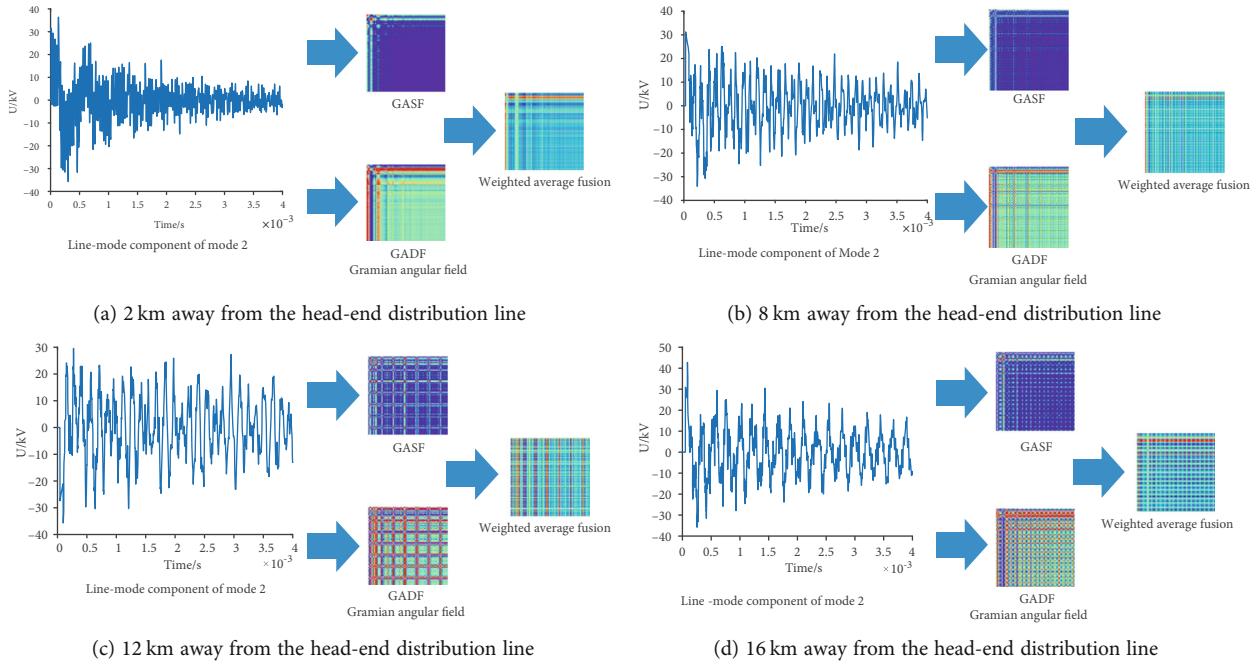

(a) 2 km away from the head-end distribution line

(b) 8 km away from the head-end distribution line

(c) 12 km away from the head-end distribution line

(d) 16 km away from the head-end distribution line

Figure 10: Two-dimensional image conversion diagrams of four kinds of fault distances.

training and iteration. It is simply impossible to complete the preparation of massive datasets by using manual simulation with multiple repetitions in the simulation process. MATLAB/SIMULINK has developed a rich operation mechanism for automation of the simulation process in order to relieve users from the burden of multiple identical repetitions of simulation so that users can realize model customization and simulation batching, and this paper selects MATLAB/SIMULINK for batching and automation of different types of fault simulation. We used the hybrid line consisting of cable and aerial wire to acquire data. The structure map of the hybrid line is shown in Figure 9, with a total line length of 20 km. The sampling frequency is 1 MHz. The simulations and deep learning have been performed using i7-10875H CPU, NVIDIA Geforce RTX 2060 with Max-Q Design, 64-bit operating system.

The zero and positive sequence parameters of the aerial wire are listed as

$$R_0 = 0.251\,\Omega/\text{km}, L_0 = 4.560 \times 10^{-3}\ \text{H/km},$$
$$C_0 = 0.0056 \times 10^{-6}\ \text{F/km}, R_1 = 0.178\,\Omega/\text{km},$$
$$L_1 = 1.250 \times 10^{-3}\ \text{H/km}, C_1 = 0.0098 \times 10^{-6}\ \text{F/km}. \quad (11)$$

The zero and positive sequence parameters of the cable line are listed as

$$R_0 = 2.750\,\Omega/\text{km}, L_0 = 1.118 \times 10^{-3}\ \text{H/km},$$
$$C_0 = 0.390 \times 10^{-6}\ \text{F/km}, R_1 = 0.278\,\Omega/\text{km},$$
$$L_1 = 0.265 \times 10^{-3}\ \text{H/km}, C_1 = 0.438 \times 10^{-6}\ \text{F/km}. \quad (12)$$

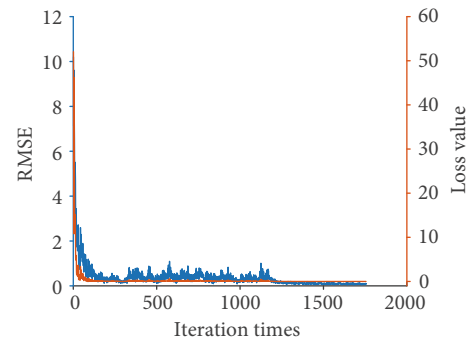

Figure 11: RMSE and loss curve of the CNN model.

Table 3 provides the parameters of the training samples, including fault types, sample size, ground resistance, and fault close angle.

5.2. Results of Signal-to-Image Conversion. Figure 10 provides two-dimensional image conversion diagrams of four kinds of fault distances. As seen from Figure 10, the 1D line-mode component can be mapped into the color, point, line, and other characteristic parameters of the 2D image. In the fusion images, texture information and color distribution show different characteristic parameters with different fault distances. The traditional analytical method needs to detect the traveling wave head and needs to know the traveling wave speed. But both are difficult to identify in the traveling wave. The mapping of the GAF coding method on the time series can possess uniqueness. The line-mode component can be encoded by GAF, which can produce the fault graph of obvious characteristics. Then, the fault distance can be obtained by regression prediction of fault feature maps using the convolution neural network.

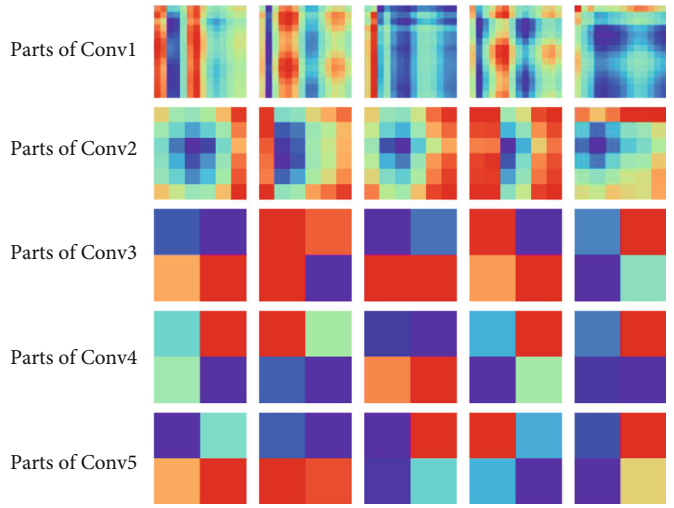

Figure 12: Visualization of features of each layer of convolution.

Table 4: Fault location results under different fault conditions.

Fault close angle	Fault types	Fault distance (km)	Location result (km)	Range error (km)
30°	AG	2.5	2.6015	0.1015
		3.8	3.6464	-0.1536
30°	BG	6	6.1125	0.1125
		8.5	8.5372	0.0372
30°	CG	3.5	3.5934	0.0934
		10.5	10.4977	-0.0023
90°	AG	11.2	11.2676	0.0676
		15.6	15.7050	0.1050
90°	G	1.6	1.6304	0.0304
		6.6	6.5188	-0.0812
90°	CG	7.6	7.4203	-0.1797
		16.8	16.7595	-0.0405
120°	AG	5.1	5.1559	0.0559
		10.3	10.3953	0.0953
120°	BG	3.5	3.4825	-0.0175
		18.5	18.4629	-0.0371
120°	CG	11.5	11.5596	0.0596
		13.9	13.8692	-0.0308
150°	AG	1.0	0.9247	-0.0753
		11.5	11.6639	0.1639
150°	BG	13.4	13.5175	0.1175
		16.6	16.7541	0.1541
150°	CG	3.5	3.4625	-0.0375
		12.3	12.4579	0.1579

5.3. Result Analysis of CNN. Figure 11 provides the root mean squared error (RMSE) and loss curve of the CNN model. As seen from Figure 11, RMSE and loss values can decrease rapidly with increasing training steps, and all finally tend to zero, indicating that the fault location model has fast convergence speed, high stability, and high prediction precision. The model has a good training process.

Figure 12 provides the visualization of the features of each layer of the convolution. In extracting image features, each convolutional kernel is equipment to a feature extractor. Different levels of convolution kernels can extract different feature information. Different layers have different abilities to learn characteristics and can extract images with more abstract features. The anterior convolution kernel in CNN can extract the bottommost image features, such as color features and texture features. As the number of the convolutional layers increases continuously, the range of feature images becomes smaller. When the convolution layers are accumulated continuously, the convolutional kernels gradually start to extract the abstract features that are more complicated and have a higher identification degree.

5.4. Result Analysis of Testing Samples. Table 4 provides fault location results under different fault conditions. From Table 4, it is easy to know that the test results have higher judging accuracy. The range error is relatively small. This method can fully utilize the convolution neural network to extract the features of the image generated by blending the GASF matrix and GADF matrix. This method avoids the problematic points in the wave head identification and traveling-wave velocity estimation. Compared to traditional traveling wave distance measurement, the proposed method has some advantages in the ranging accuracy.

Figure 13 provides the evaluation indexes for three input methods under 500 testing samples. From Figure 13, it is easy to know that the explained variance score (EVS) and decision coefficient (DC) are near 1, indicating that three input methods all have good fitting results. However, the root means square error (RMSE) and mean absolute error (MAE) of image fusion is the smallest, indicating that image fusion-CNN has the preferable fault location effect.

Different phase-mode transformation matrixes also influence the effect of fault distance measurement. Table 5 provides the results of fault location under different phase-

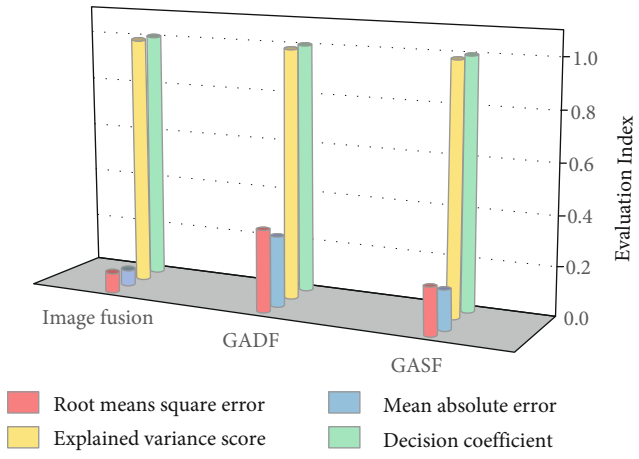

Figure 13: Evaluation indexes for three input methods.

Table 5: Results of fault location under different phase-mode transformation matrixes.

Fault types	Fault distance (km)	Clarke (km)	Range error of Clarke (km)	This paper (km)	Range error of this paper (km)
	0.5	0.7350	0.2350	0.5554	0.0554
	1.0	1.0652	0.0652	0.8966	-0.1034
	2.2	2.5064	0.3064	2.4352	0.2352
AG	4.5	491	0.3991	4.4899	-0.0101
	5.5	6.7651	1.2651	5.5770	0.0770
	6.0	6.6974	0.6974	6.0206	0.0206
	7.9	7.4039	-0.4961	8.0608	0.1608
	0.5	3.2778	2.7778	0.6003	0.1003
	1.0	3.8437	2.8437	0.8025	-0.1975
	2.2	3.7938	1.5938	2.3667	0.1667
BG	4.5	5.3339	0.8339	4.5479	0.0479
	5.5	5.4917	-0.0083	5.4859	-0.0141
	6.0	5.5436	-0.4564	6.0423	0.0423
	7.9	5.4927	-2.4073	8.0606	0.1606
	0.5	0.5973	0.0973	0.6811	0.1811
	1.0	0.9620	-0.0380	0.8551	-0.1449
	2.2	2.3238	0.1238	2.3071	0.1071
CG	4.5	4.7555	0.2557	4.5175	0.0175
	5.5	6.7567	1.2567	5.3396	-0.1604
	6.0	6.7053	0.7053	5.9139	-0.0861
	7.9	7.4334	-0.4666	7.8825	-0.0175

mode transformation matrixes. From Table 5, it is evident that the Clarke transformation has a poor fault location effect when the system occurs in the BG fault. The reason is that the mode 2 component of the Clarke transformation always equals zero when the system occurs in the BG fault. However, the phase-mode transformation matrix used in this paper still has a good effect on the fault location under different fault conditions.

The BP neural network, support vector machine (SVM), and extreme learning machine (ELM) are added for testing

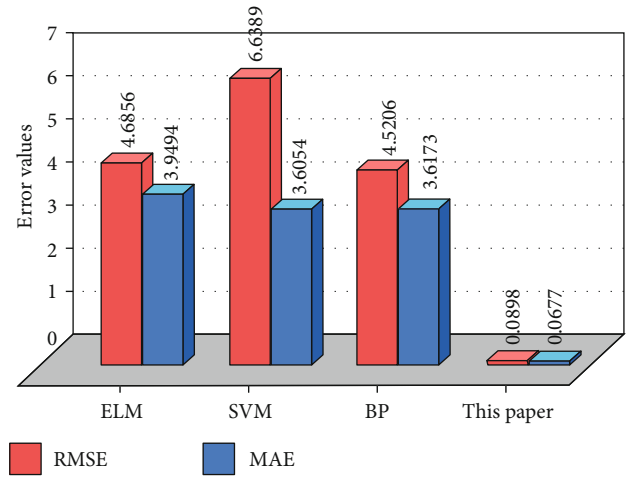

Figure 14: Evaluation results of fault location under the different diagnosis methods.

experiments. The test samples are 500 fusion images. Figure 14 provides the evaluation results of fault location under the different diagnosis methods. The RMSE and MAE of this paper are the smallest in different diagnosis methods. From Figure 14, it can be seen that this method can adaptively extract feature vectors for fault range finding.

In order to verify the effectiveness of the proposed method, three different kinds of fault location methods are compared. The fault range finding results are shown in Table 6. Compared with other methods, the proposed method has the smallest distance-measuring error. This is because the proposed method does not require detection of the wave head and speed of the traveling wave. This method features intelligence and does not require manual mining of fault features.

6. Conclusions

In this paper, a new fault distance measuring in the nonsolid-earthed network based on spatial domain image fusion and convolution neural network is proposed and verified:

(1) The 1D line-mode component can be converted into the 2D image by GASF and GADF. Imaging line-mode components can enhance the unviewable features of the 1D line-mode component. The fault location using the fusion images can have the best effect

(2) Compared with different diagnosis methods, CNN can automatically extract the features of the fusion images and eliminate the influence of human factors

(3) Compared to traditional traveling wave distance measurement, the proposed method can avoid the problematic points in the wave head identification and traveling-wave velocity estimation. The fault location in the paper still has minor errors under different fault conditions

Table 6: Results of fault location under three different kinds of methods.

Fault types	Fault distance (km)	Fault location error (km)		
		Paper [32]	Paper [33]	Proposed method
AG	1.2	0.968	2.374	0.032
AG	3.6	1.126	1.562	0.152
BG	5	1.413	1.827	0.098
BG	4.3	1.237	1.635	0.101
CG	6.2	1.819	2.078	0.195
CG	2.6	1.068	1.235	0.097

Notations

SCGS: Small current grounding system
CNN: Convolutional neural network
GAF: Gramian angular field
GASF: Gramian angular summation field
GADF: Gramian angular difference field
RMSE: Root mean squared error
MAE: Mean absolute error
EVS: Explained variance score
DC: Decision coefficient
ELM: Extreme learning machine
SVM: Support vector machine.

Data Availability

The data used to support the findings of this study are available from the corresponding author upon request.

Conflicts of Interest

The authors declare that they have no conflicts of interest.

Acknowledgments

The work was supported by the National Key R&D Program of China (2018YFF01011900).

References

[1] X. Wang, J. Gao, G. Song, Q. Cheng, X. Wei, and Y. Wei, "Faulty line selection method for distribution network based on variable scale bistable system," *Journal of Sensors*, vol. 2016, Article ID 7436841, 17 pages, 2016.

[2] L. Niu, G. Wu, and Z. Xu, "Single-phase fault line selection in distribution network based on signal injection method," *IEEE Access*, vol. 9, pp. 2156–21578, 2021.

[3] J. Huang, S. Ge, J. Han et al., "A diagnostic method for distribution networks based on power supply safety standards," *Protection and Control of Modern Power Systems*, vol. 1, no. 9, pp. 1–8, 2016.

[4] R. H. Salim, K. C. O. Salim, and A. S. Bretas, "Further improvements on impedance-based fault location for power distribution systems," *IET Generation, Transmission & Distribution*, vol. 5, no. 4, pp. 467–478, 2011.

[5] N. I. Elkalashy, N. A. Sabiha, and M. Lehtonen, "Earth fault distance estimation using active traveling waves in energized compensated MV networks," *IEEE Transactions on Power Delivery*, vol. 30, no. 2, pp. 836–843, 2015.

[6] Y. Liao, "Generalized fault-location methods for overhead electric distribution systems," *IEEE Transactions on Power Delivery*, vol. 26, no. 1, pp. 53–64, 2011.

[7] K. Sun, Q. Chen, and Z. Gao, "An automatic faulted line section location method for electric power distribution systems based on multisource information," *IEEE Transactions on Power Delivery*, vol. 31, no. 4, pp. 1542–1551, 2016.

[8] N. Sapountzoglou, J. Lago, and B. Raison, "Fault diagnosis in low voltage smart distribution grids using gradient boosting trees," *Electric Power Systems Research*, vol. 182, pp. 1–12, 2020.

[9] J. H. Teng, W. H. Huang, and S. W. Luan, "Automatic and fast faulted line-section location method for distribution systems based on fault indicators," *IEEE Transactions on Power Systems*, vol. 29, no. 4, pp. 1653–1662, 2014.

[10] Z. Qi, S. Zhang, and Z. Haung, "Traveling wave fault location technology for hybrid lines in distribution network based on disturbance signal injection at busbar," *Automation of Electric Power Systems*, vol. 43, no. 13, pp. 124–130, 2019.

[11] F. Kong, Z. Hao, and B. Zhang, "A novel traveling-wave-based main protection scheme for ±800 kV UHVDC bipolar transmission lines," *IEEE Transactions on Power Delivery*, vol. 31, no. 5, pp. 2159–2168, 2016.

[12] I. M. Karmacharya and R. Gokaraju, "Fault location in ungrounded photovoltaic system using wavelets and ANN," *IEEE Transactions on Power Delivery*, vol. 33, no. 2, pp. 549–559, 2018.

[13] G. Qi, Z. Zhu, K. Erqinhu, Y. Chen, Y. Chai, and J. Sun, "Fault-diagnosis for reciprocating compressors using big data and machine learning," *Simulation Modelling Practice and Theory*, vol. 80, pp. 104–127, 2018.

[14] X. Huang, G. Qi, N. Mazur, and Y. Chai, "Deep residual networks-based intelligent fault diagnosis method of planetary gearboxes in cloud environments," *Simulation Modelling Practice and Theory*, vol. 116, pp. 1–16, 2022.

[15] G. Luo, C. Yao, Y. Liu, Y. Tan, J. He, and K. Wang, "Stacked auto-encoder based fault location in VSC-HVDC," *IEEE Access*, vol. 6, pp. 33216–33224, 2018.

[16] M. Mirzaei, B. Vahidi, and S. H. Hosseinian, "Accurate fault location and faulted section determination based on deep learning for a parallel-compensated three-terminal transmission line," *IET Generation, Transmission & Distribution*, vol. 13, no. 13, pp. 2770–2778, 2019.

[17] G. Luo, Y. Tan, M. Li, M. Cheng, Y. Liu, and J. He, "Stacked auto-encoder-based fault location in distribution network," *IEEE Access*, vol. 8, pp. 28043–28053, 2020.

[18] Y. Wang, T. Zheng, C. Yang, and L. Yu, "Traveling-wave based fault location for phase-to-ground gault in non-effectively earthed distribution networks," *Energies*, vol. 13, no. 19, pp. 1–15, 2020.

[19] Y. Shi, T. Zheng, and C. Yang, "Reflected traveling wave based single-ended fault location in distribution networks," *Energies*, vol. 13, no. 15, pp. 1–19, 2020.

[20] R. Muzzammel, "Traveling waves-based method for fault estimation in HVDC transmission system," *Energies*, vol. 12, no. 19, pp. 1–31, 2019.

[21] S. Wang, D. Zhao, J. Yuan, and Y. Gao, "New phase-mode transformation matrix for fault location of double-circuit

transmission lines," *Journal of Xi'an University of Technology*, vol. 36, no. 3, pp. 432–438, 2020.

[22] L. Shang, Y. Liu, S. Wang, and W. Liang, "A new phase mode transformation matrix," in *Proceedings of the 36th Chinese Control Conference*, vol. 26-28, pp. 10767–10770, Dalian, Chian, 2017.

[23] H. Zhou and C. Kan, "Tensor-based ECG anomaly detection toward cardiac monitoring in the internet of health things," *Sensors*, vol. 21, no. 12, pp. 1–17, 2021.

[24] Z. Wang and T. Oates, "Imaging time-series to improve classification and imputation," in *Proceedings of the Twenty-Fourth International Joint Conference on Artificial Intelligence (IJCAI 2015)*, vol. 25–31, pp. 3939–3945, Buenos Aires, Argentina, 2015.

[25] C. L. Yang, Z. X. Chen, and C. Y. Yang, "Sensor classification using convolutional neural network by encoding multivariate time series as two-dimensional colored images," *Sensors*, vol. 20, no. 1, pp. 1–15, 2019.

[26] Y. Bai, J. Yang, J. Wang, and Q. Li, "Intelligent diagnosis for railway wheel flat using frequency-domain Gramian angular field and transfer learning network," *IEEE Access*, vol. 8, pp. 105118–105126, 2020.

[27] Y. Zhang, L. Duan, and M. Duan, "A new feature extraction approach using improved symbolic aggregate approximation for machinery intelligent diagnosis," *Measurement*, vol. 133, pp. 468–478, 2019.

[28] Y. LeCun, Y. Bengio, and G. Hinton, "Deep learning," *Nature*, vol. 521, no. 7553, pp. 436–444, 2015.

[29] O. Abdel-Hamid, A.-R. Mohamed, H. Jiang, L. Deng, G. Penn, and D. Yu, "Convolutional neural networks for speech recognition," *IEEE Transactions on Audio, Speech and Language Processing*, vol. 22, no. 10, pp. 1533–1545, 2014.

[30] V. Radu, C. Tong, S. Bhattacharya et al., "Multimodal deep learning for activity and context recognition," *Proceedings of the ACM on Interactive, Mobile, Wearable and Ubiquitous Technologies*, vol. 1, no. 4, pp. 1–27, 2018.

[31] F. Zhou, L. Jin, and J. Dong, "Review of convolutional neural network," *Chinese Journal of Computers*, vol. 40, no. 6, pp. 1229–1251, 2017.

[32] Y. Wang, T. Zheng, C. Yang, and L. Yu, "Traveling-wave based fault location for phase-to-ground fault in non-effectively earthed distribution networks," *Energies*, vol. 13, no. 19, pp. 1–15, 2020.

[33] S. Hou and X. Guo, "Research on fault location of distribution lines based on the standing wave principle," *PRO*, vol. 9, no. 8, pp. 1–20, 2021.